Available online at www.sciencedirect.com
SCIENCE DIRECT®
Journal of Sound and Vibration 292 (2006) 221–241
JOURNAL OF SOUND AND VIBRATION
www.elsevier.com/locate/jsvi

An analytical model for train-induced ground vibrations from railways

A. Karlström*, A. Boström

Department of Applied Mechanics, Chalmers University of Technology, SE-412 96, Göteborg, Sweden

Received 19 January 2004; received in revised form 26 May 2005; accepted 27 July 2005
Available online 19 September 2005

Abstract

To investigate ground vibrations from railways an analytical approach is taken. The ground is modelled as a stratified half-space with linearly viscoelastic layers. On top of the ground a rectangular embankment is placed, supporting the rails and the sleepers. The rails are modelled as Euler–Bernoulli beams where the propagating forces (wheel loads) are acting and the sleepers are modelled with an anisotropic Kirchhoff plate. The solution is based on Fourier transforms in time and along the track. In the transverse direction the fields in the embankment are developed in Fourier series and in the half-space with Fourier transforms. The resulting numerical scheme is very efficient, permitting displacement fields far outside the track to be calculated. Numerical examples are given for an X2 train that operates at the site Ledsgard in Sweden. The displacements are simulated at 70 and 200 km/h and are compared with the displacements from simpler models. The simulations are also validated against measurements, with very good agreement. At 70 km/h the track displacements agree almost exactly and at 200 km/h the displacements are a very good approximation of the measurement.

1. Introduction

With the development of ever faster trains the problem with excessive ground vibrations has increased. These problems are of particular relevance when the ground consists of soft materials,

*Corresponding author. Tel.: +46 31 772 1295; fax: +46 31 772 3827.
E-mail addresses: anders.karlstrom@chalmers.se (A. Karlström), anders.bostrom@chalmers.se (A. Boström).

0022-460X/$ - see front matter © 2005 Elsevier Ltd. All rights reserved.
doi:10.1016/j.jsv.2005.07.041

such as various types of clay. In these materials the shear wave velocity may be as low as 30–40 m/s, and is thus lower than typical train speeds. A well-documented case with large vibrations due to high speed trains occurred at Ledsgard in Sweden [1–4].

The interest in modelling ground vibrations has increased in recent years, mainly because of the problems with high speed trains. The mathematical problem with a moving point force on an elastic half-space is an old problem, see Ref. [5] for the stationary problem in a layered viscoelastic configuration and an extensive review. Recent contributions with a non-stationary load include Refs. [6,7].

To include the stiffness of the embankment and rails, a model with a beam on an elastic half-space is common. Dieterman and Metrikine [8] determine the critical speed of a uniformly moving point load and give further references. Recently, Madshus and Kaynia [3] and Kaynia et al. [2] used a viscoelastic beam treated by finite elements on an analytical layered half-space and favourably compare the results with the measurements at Ledsgard. Takemiya [4] uses an analytical model with an Euler–Bernoulli beam on a layered viscoelastic half-space, which also compares the results with the measurements at Ledsgard with good agreement. Also Krylov and Ferguson [9] and Sheng et al. [10] use similar models, the latter for considering a time harmonic load.

The more or less analytical methods mentioned so far have the advantage of leading to fast numerical computations and to a natural modelling of the infinite domains (radiation conditions). But the geometries of necessity are rather limited, although this is primarily a limitation at higher frequencies. Another limitation is that analytical methods are restricted to linear phenomena. An alternative is of course to employ FEM or some other discretization method. This allows for arbitrary geometries and for nonlinear effects. However, the infinite domains must be treated in some way, e.g. by absorbing or radiation boundary conditions. Another drawback is the computational time which can be very long (days or more). An example of the application of FEM is given by Ekevid and Wiberg [11], where the scaled boundary finite element method proposed by Wolf and Song [12] is used to treat the infinite domain. Another limitation of FEM, that is apparent from their paper, is that the discretized region is small, in this case 40 m in length (with a 107 m long train) and less than that in the transverse direction. Thus the response is only obtained in a region quite close to the train.

In the present paper, a more refined analytical model is introduced. This model includes an embankment of finite width and height that is placed on a stratified half-space with viscoelastic layers. The embankment is also modelled as a viscoelastic material. The two rails are modelled as beams on top of the embankment and in addition to the vertical movement also the transverse and longitudinal displacements are taken into account. Thus, the rails are governed by Euler–Bernoulli's equation in both the vertical and transverse directions but by the rod equation in the longitudinal direction. No torsion is included. The sleepers are also placed on top of the embankment and are governed by an anisotropic Kirchhoff plate. Comparisons are made with simpler models (which can be obtained as limits) and with measurements.

The plan of the present paper is as follows. In Section 2 the problem is formulated and it is in particular pointed out that the boundary conditions on the vertical sides of the embankment are of a special type with vanishing tangential stresses but vanishing normal displacement. In Section 3, these boundary conditions are seen to enable a Fourier series representation of the displacements in the transverse direction in the embankment. Together with Fourier transforms

this leads to a rather straightforward solution procedure. The validity of the boundary conditions is investigated with finite elements in Section 4 and the constraint on the normal displacement is seen to have little effect on the results when it is compared to the natural boundary conditions. Finally, in Section 5 some numerical results are presented and the displacements are compared to measurements.

2. Problem formulation

To model a railway track, a rectangular embankment with the outer dimensions $2a \times d$ is situated on the surface of a layered ground, see Fig. 1. On top of the embankment, the rails are modelled as two Euler–Bernoulli beams with the width c at the positions $\pm b_R$ and the sleepers as an anisotropic Kirchhoff plate with the dimensions $2b_S \times h$. The ground consists of n layers, which are positioned with the coordinates $d_1 - d_{n-1}$. Each wheel is treated as a point load acting on the rail: $F = F_0\delta(x - \int_0^t V(s)\,\mathrm{d}s)$. F_0 is the amplitude, $V(t)$ the time-dependent velocity, x the coordinate along the track and t the time. The displacement components in the embankment and in the layered ground are $\mathbf{u}_j = \{u_j, v_j, w_j\}$, where u_j, v_j and w_j are the cartesian components in the x, y and z direction, respectively. The index j represents the embankment ($j = e$) and the ground layers ($j = 1, 2, \ldots, n$). With similar use of notation, the material parameters are defined with the density ρ_j and the Lamé constants with hysteretic damping λ_j and μ_j.

The displacements in the embankment and in each layer are governed by the elastodynamic equations of motion:

$$(\lambda_j + 2\mu_j)\nabla(\nabla \cdot \mathbf{u}_j) - \mu_j \nabla \times (\nabla \times \mathbf{u}_j) = \rho_j \ddot{\mathbf{u}}_j \tag{1}$$

and the traction on a plane with the normal direction $\mathbf{e}_k$ ($k = x, y, z$) is given by

$$\mathbf{t}_j^{(\mathbf{e}_k)} = \lambda_j \mathbf{e}_k \nabla \cdot \mathbf{u}_j + 2\mu_j \partial_k \mathbf{u}_j + \mu_j \mathbf{e}_k \times (\nabla \times \mathbf{u}_j). \tag{2}$$

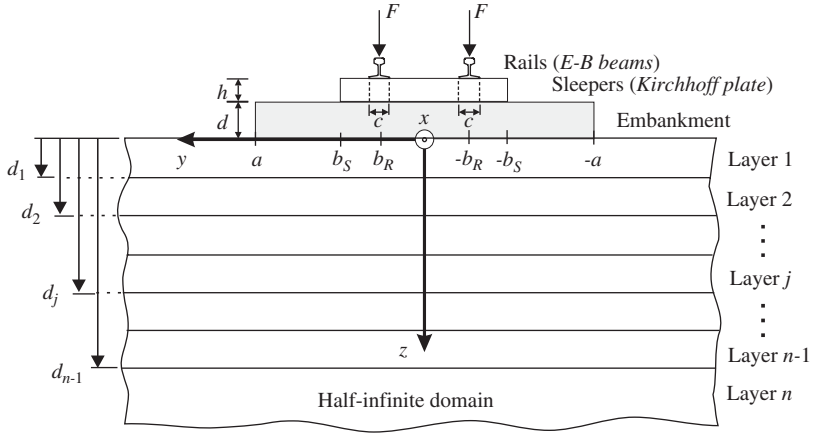

Fig. 1. A cross section of the model showing geometrical and material properties and the applied wheel loads. The rails and the sleepers are introduced as boundary conditions on top of the embankment.

At each interface between two layers, i.e. at the coordinates $z = d_j$ between layer j and $j+1$, the displacement and traction vectors are continuous:

$$\mathbf{u}_j = \mathbf{u}_{j+1}, \quad z = d_j, \tag{3}$$

$$\mathbf{t}_j^{(\mathbf{e}_z)} = \mathbf{t}_{j+1}^{(\mathbf{e}_z)}, \quad z = d_j. \tag{4}$$

On the top surface the traction must vanish, except for the region under the embankment where the displacement and traction vectors are continuous:

$$\mathbf{u}_1 = \mathbf{u}_e, \quad |y| < a, \quad z = 0, \tag{5}$$

$$\mathbf{t}_1^{(\mathbf{e}_z)} = \begin{cases} \mathbf{t}_e^{(\mathbf{e}_z)}, & |y| < a, \ z = 0, \\ 0, & |y| > a, \ z = 0. \end{cases} \tag{6}$$

To enable a series expansion of the displacement field in the embankment, the boundary conditions on the sides of the embankment must be designed in a special way:

$$\begin{cases} v_e = 0, & |y| = a, \ -d < z < 0, \\ \sigma_{xye} = 0, & |y| = a, \ -d < z < 0, \\ \sigma_{zye} = 0, & |y| = a, \ -d < z < 0. \end{cases} \tag{7}$$

The two conditions on the shear stresses are the natural ones, but the constraint on the normal displacement component v_e is unphysical. The reason for this choice is mathematical, because these conditions imply the following simpler ones:

$$\begin{cases} v_e = 0, & |y| = a, \ -d < z < 0, \\ \partial_y u_e = 0, & |y| = a, \ -d < z < 0, \\ \partial_y w_e = 0, & |y| = a, \ -d < z < 0. \end{cases} \tag{8}$$

It is seen in Section 4 that the constraint on the normal displacement gives very good approximations of the vertical displacements on top of and besides the embankment when the rails are loaded vertically.

On top of the embankment the two rails are placed. They are characterized by the cross-sectional area A_b, the modulus of elasticity E_b, the mass density ρ_b and the moment of inertia about the y and z axis I_{yb} and I_{zb} (subscript b denotes beam). In the transverse direction they are governed by Euler–Bernoulli's equation and in the longitudinal direction by the rod equation.

It is recently shown by Vostroukhov and Metrikine [13] that the vertical displacement due to train passage over a track with discrete sleeper positions is almost identical to the results when the sleepers are uniformly distributed along the track. Hence the mass and stiffness from the sleepers are accounted for by introducing a transversely isotropic Kirchhoff plate [14]. The shear stiffness and the Young's modulus in the x direction should both be equal to zero if the rails are supported by sleepers. However, a slab track carries forces in the longitudinal direction via the sleepers. A transversely isotropic plate model is able to describe both situations. The plate material has a mass density ρ_s, a modulus of elasticity E_{sk} and Poisson's ratio v_{syz} in the y–z plane and E_{sx} in the x direction and v_{sxk} in the x–k plane, where k represents all directions perpendicular to the x direction. In the x direction the shear modulus is G_{sx} and in the isotropic y–z plane it is simply

$G_{sk} = E_{sk}/2(1 + v_{syz})$. Note that $v_{sxk}E_{sx} = v_{skx}E_{sk}$ due to symmetry of the stiffness tensor. On the free surface next to the plate, i.e. at $b_S \leqslant y < a$, the traction vanishes.

The normal and transverse components of the traction on top of the embankment thus satisfy the boundary conditions:

$$\sigma_{zze} = \begin{cases} J_1\ddot{w}_e + J_2\partial_x^4 w_e + J_3\partial_x^2\partial_y^2 w_e + J_4\partial_y^4 w_e, & |y| < b_S, \quad |y| \notin [b_R \pm c/2], \\ I_1\ddot{w}_e + I_2\partial_x^4 w_e + I_3\partial_x^2\partial_y^2 w_e + I_4\partial_y^4 w_e - F/c, & |y| \in [b_R \pm c/2], \\ 0, & b_S \leqslant |y| < a, \end{cases} \tag{9}$$

$$\sigma_{yze} = \begin{cases} (\rho_b A_b\ddot{v}_e + E_b I_{zb}\partial_x^4 v_e)/c, & |y| \in [b_R \pm c/2], \\ 0, & |y| \notin [b_R \pm c/2], \end{cases} \tag{10}$$

where

$$\begin{aligned} I_1 &= J_1 + \frac{\rho_b A_b}{c}, & J_1 &= \rho_s h, \\ I_2 &= J_2 + \frac{E_b I_{yb}}{c}, & J_2 &= \frac{h^3}{12}\left(\frac{E_{sx}^2}{E_{sx} - E_{sk}v_{sxk}^2}\right), \\ I_3 &= J_3, & J_3 &= \frac{h^3}{6}\left(\frac{E_{sk}E_{sx}v_{sxk}}{E_{sx} - E_{sk}v_{sxk}^2} + 2G_{sx}\right), \\ I_4 &= J_4, & J_4 &= \frac{h^3}{12}\left(\frac{E_{sk}E_{sx}}{E_{sx} - E_{sk}v_{sxk}^2}\right). \end{aligned}$$

In the longitudinal direction the shear stress, σ_{xze}, accounts for the coupling to the rails via the rod equation:

$$\sigma_{xze} = \begin{cases} (\rho_b A_b\ddot{u}_e - E_b A_b\,\partial_x^2 u_e)/c, & |y| \in [b_R \pm c/2], \\ 0, & |y| \notin [b_R \pm c/2]. \end{cases} \tag{11}$$

The boundary conditions (9)–(11) are valid for $z = -d$ and all x.

3. Exact solution

From the geometry of the problem, natural ways to represent the solution follow. It is convenient to apply Fourier transforms with respect to t and x, where the corresponding transform variables are denoted ω, which is the angular frequency, and q, which is the wavenumber in the x direction. The doubly transformed fields are denoted by a hat.

Analytical solutions to the equations of motion (1) are obtained by decomposing the displacement fields in three scalar potentials in the embankment ($j = e$) and in the ground layers ($j = 1, 2, \ldots, n$):

$$\mathbf{u}_j = \nabla\varphi_j + \nabla \times (\mathbf{e}_z\psi_{SHj}) + \nabla \times \nabla \times (\mathbf{e}_z\psi_{SVj}). \tag{12}$$

Here φ_j, ψ_{SHj} and ψ_{SVj} are potentials for longitudinal, horizontal transverse and vertical transverse waves which satisfy scalar wave equations.

3.1. Solution in the ground

In the layered ground a Fourier transform in y makes it possible to represent the displacement fields by employing the potentials:

$$\hat{\varphi}_j = \frac{1}{2\pi}\int_{-\infty}^{\infty}(A_{jd}\,\mathrm{e}^{\mathrm{i}h_{pj}(z-d_{j-1})} + A_{ju}\,\mathrm{e}^{-\mathrm{i}h_{pj}(z-d_j)})\,\mathrm{e}^{\mathrm{i}py}\,\mathrm{d}p, \tag{13}$$

$$\hat{\psi}_{SHj} = \frac{1}{2\pi}\int_{-\infty}^{\infty}(B_{jd}\,\mathrm{e}^{\mathrm{i}h_{sj}(z-d_{j-1})} + B_{ju}\,\mathrm{e}^{-\mathrm{i}h_{sj}(z-d_j)})\,\mathrm{e}^{\mathrm{i}py}\,\mathrm{d}p, \tag{14}$$

$$\hat{\psi}_{SVj} = \frac{1}{2\pi}\int_{-\infty}^{\infty}(C_{jd}\,\mathrm{e}^{\mathrm{i}h_{sj}(z-d_{j-1})} + C_{ju}\,\mathrm{e}^{-\mathrm{i}h_{sj}(z-d_j)})\,\mathrm{e}^{\mathrm{i}py}\,\mathrm{d}p, \tag{15}$$

where p is the transform variable to y. $A_{jd} = A_{jd}(p)$, $A_{ju} = A_{ju}(p)$, $B_{jd} = B_{jd}(p)$, $B_{ju} = B_{ju}(p)$, $C_{jd} = C_{jd}(p)$ and $C_{ju} = C_{ju}(p)$ are the amplitudes of the down-going (subscript d) and up-going (subscript u) P, SH and SV waves, respectively. The wavenumbers are $k_{pj} = \omega/c_{pj}$ and $k_{sj} = \omega/c_{sj}$, where the wave speeds are given by $c_{pj} = ((\lambda_j + 2\mu_j)/\rho_j)^{1/2}$ and $c_{sj} = (\mu_j/\rho_j)^{1/2}$. Corresponding wavenumbers in the z direction are $h_{pj} = (k_{pj}^2 - q^2 - p^2)^{1/2}$ and $h_{sj} = (k_{sj}^2 - q^2 - p^2)^{1/2}$, where $\mathrm{Im}\,h_{pj} \geqslant 0$ and $\mathrm{Im}\,h_{sj} \geqslant 0$. In the last half-infinite layer ($j = n$) there are no reflected waves, i.e. $A_{nu} = 0$, $B_{nu} = 0$ and $C_{nu} = 0$, and the radiation condition with down-going or evanescent waves has been applied. The d_{j-1} and d_j in the exponents are crucial as they prevent exponential growth. With this choice the absolute value of the exponential functions never exceeds one. When $j = 1$ by definition: $d_0 = 0$.

It is trivial to obtain the displacement fields and the stresses by employing Eqs. (13)–(15) together with Eqs. (12) and (2).

3.2. Solution in the embankment

As mentioned, the displacement field in the embankment ($j = e$) can be developed in trigonometric series and must satisfy the boundary conditions along the sides of embankment (8). Due to the symmetric loading the field $\mathbf{u}_e$ is symmetric about $y = 0$, which means that u_e and w_e are even and v_e is odd. Hence they are developed in Fourier cosine and Fourier sine series, with wavenumber $p_m = m\pi/a$ in the y direction. This gives the following choice for the potentials in Eq. (12):

$$\hat{\varphi}_e = \sum_{m=0}^{\infty}(D_{1m}\sin h_{pm}z + E_{1m}\cos h_{pm}z)\cos p_m y, \tag{16}$$

$$\hat{\psi}_{SHe} = \sum_{m=1}^{\infty}(D_{2m}\sin h_{sm}z + E_{2m}\cos h_{sm}z)\sin p_m y, \tag{17}$$

$$\hat{\psi}_{SVe} = \sum_{m=0}^{\infty} (E_{3m} \sin h_{sm} z - D_{3m} \cos h_{sm} z) \cos p_m y. \tag{18}$$

D_{nm} and E_{nm} are unknown amplitudes, where $n = 1, 2$ and 3 give the amplitudes for the P, SH and SV waves, respectively. The wavenumbers are similar to those in the half-space, but with subscript e to denote the embankment: $k_{pe} = \omega/c_{pe}$ and $k_{se} = \omega/c_{se}$. Here the wave speeds are given by $c_{pe} = ((\lambda_e + 2\mu_e)/\rho_e)^{1/2}$ and $c_{se} = (\mu_e/\rho_e)^{1/2}$ and the wavenumbers in the z direction are $h_{pm} = (k_{pe}^2 - q^2 - p_m^2)^{1/2}$ and $h_{sm} = (k_{se}^2 - q^2 - p_m^2)^{1/2}$, where the roots are defined so that $\operatorname{Im} h_{pm} \geqslant 0$ and $\operatorname{Im} h_{sm} \geqslant 0$.

Similar to the layers in the ground, the displacement field can easily be determined employing Eqs. (16)–(18) together with Eq. (12):

$$\hat{u}_e = \sum_{m=0}^{\infty} \hat{u}_m(z) \cos p_m y, \tag{19}$$

$$\hat{v}_e = \sum_{m=1}^{\infty} \hat{v}_m(z) \sin p_m y, \tag{20}$$

$$\hat{w}_e = \sum_{m=0}^{\infty} \hat{w}_m(z) \cos p_m y, \tag{21}$$

where

$$\hat{u}_m(z) = \sum_{n=1}^{3} \alpha_{nm} (D_{nm} \sin k_{nm} z + E_{nm} \cos k_{nm} z), \tag{22}$$

$$\hat{v}_m(z) = \sum_{n=1}^{3} \beta_{nm} (D_{nm} \sin k_{nm} z + E_{nm} \cos k_{nm} z), \tag{23}$$

$$\hat{w}_m(z) = \sum_{n=1}^{3} \gamma_{nm} (D_{nm} \cos k_{nm} z - E_{nm} \sin k_{nm} z). \tag{24}$$

The coefficients α_{nm}, β_{nm}, γ_{nm} and k_{nm} are tabulated in Table 1.

Table 1
Displacement coefficients in embankment

$n =$	1	2	3
α_{nm}	$\mathrm{i}q$	p_m	$\mathrm{i}qh_{sm}$
β_{nm}	$-p_m$	$-\mathrm{i}q$	$-p_m h_{sm}$
γ_{nm}	h_{pm}	0	$-(p_m^2 + q^2)$
k_{nm}	h_{pm}	h_{sm}	h_{sm}

The z components of the stresses are used in the boundary conditions and are derived using Eq. (2):

$$\hat{\sigma}_{xz\,e} = \sum_{m=0}^{\infty} \hat{\sigma}_{xz\,m}(z) \cos p_m y, \tag{25}$$

$$\hat{\sigma}_{yz\,e} = \sum_{m=0}^{\infty} \hat{\sigma}_{yz\,m}(z) \sin p_m y, \tag{26}$$

$$\hat{\sigma}_{zz\,e} = \sum_{m=0}^{\infty} \hat{\sigma}_{zz\,m}(z) \cos p_m y, \tag{27}$$

where

$$\hat{\sigma}_{xz\,m}(z) = \sum_{n=1}^{3} \mu_e \xi_{nm} (D_{nm} \cos k_{nm} z - E_{nm} \sin k_{nm} z), \tag{28}$$

$$\hat{\sigma}_{yz\,m}(z) = \sum_{n=1}^{3} \mu_e \zeta_{nm} (D_{nm} \cos k_{nm} z - E_{nm} \sin k_{nm} z), \tag{29}$$

$$\hat{\sigma}_{zz\,m}(z) = \sum_{n=1}^{3} \mu_e \eta_{nm} (D_{nm} \sin k_{nm} z + E_{nm} \cos k_{nm} z). \tag{30}$$

The coefficients ξ_{nm}, ζ_{nm} and η_{nm} collect the resulting coefficients from the differentiations in Eq. (2):

$$\xi_{nm} = k_{nm}\alpha_{nm} + \mathrm{i}q\gamma_{nm}, \tag{31}$$

$$\zeta_{nm} = k_{nm}\beta_{nm} - p_m\gamma_{nm}, \tag{32}$$

$$\eta_{nm} = ((k_{se}/k_{pe})^2 - 2)(\mathrm{i}q\alpha_{nm} + p_m\beta_{nm}) - (k_{se}/k_{pe})^2 k_{nm}\gamma_{nm}. \tag{33}$$

3.3. General solution procedure

To obtain a solution to the unknowns in the ground expressed in the constants in the embankment, the interfacial conditions (3)–(4) and the boundary condition (6) are used. The interfacial conditions in Eq. (3) give

$$\mathrm{i}qA_j(d_j) + \mathrm{i}pB_j(d_j) - qh_{sj}C_j(d_j) = \mathrm{i}qA_{j+1}(d_j) + \mathrm{i}pB_{j+1}(d_j) - qh_{sj+1}C_{j+1}(d_j), \tag{34}$$

$$\mathrm{i}p\,A_j(d_j) - \mathrm{i}qB_j(d_j) - ph_{sj}C_j(d_j) = \mathrm{i}pA_{j+1}(d_j) - \mathrm{i}qB_{j+1}(d_j) - ph_{sj+1}C_{j+1}(d_j), \tag{35}$$

$$\mathrm{i}h_{pj}\widetilde{A}_j(d_j) + (q^2+p^2)\widetilde{C}_j(d_j) = \mathrm{i}h_{pj+1}\widetilde{A}_{j+1}(d_j) + (q^2+p^2)\widetilde{C}_{j+1}(d_j) \tag{36}$$

and the conditions in Eq. (4) give:

$$\begin{aligned}&\mu_j(-2qh_{pj}\widetilde{A}_j(d_j) - ph_{sj}\widetilde{B}_j(d_j) + \mathrm{i}q(k_{sj}^2 - 2h_{sj}^2)\widetilde{C}_j(d_j))\\&\quad = \mu_{j+1}(-2qh_{pj+1}\widetilde{A}_{j+1}(d_j) - ph_{sj+1}\widetilde{B}_{j+1}(d_j)\\&\qquad + \mathrm{i}q(k_{sj+1}^2 - 2h_{sj+1}^2)\widetilde{C}_{j+1}(d_j)),\end{aligned} \tag{37}$$

$$\begin{aligned}&\mu_j(-2ph_{pj}\widetilde{A}_j(d_j) + qh_{sj}\widetilde{B}_j(d_j) + \mathrm{i}p(k_{sj}^2 - 2h_{sj}^2)\widetilde{C}_j(d_j))\\&\quad = \mu_{j+1}(-2ph_{pj+1}\widetilde{A}_{j+1}(d_j) + qh_{sj+1}\widetilde{B}_{j+1}(d_j)\\&\qquad + \mathrm{i}p(k_{sj+1}^2 - 2h_{sj+1}^2)\widetilde{C}_{j+1}(d_j)),\end{aligned} \tag{38}$$

$$\begin{aligned}&\mu_j((k_{sj}^2 - 2h_{sj}^2)A_j(d_j) + 2\mathrm{i}h_{sj}(p^2+q^2)C_j(d_j))\\&\quad = \mu_{j+1}((k_{sj+1}^2 - 2h_{sj+1}^2)A_{j+1}(d_j) + 2\mathrm{i}h_{sj+1}(p^2+q^2)C_{j+1}(d_j)),\end{aligned} \tag{39}$$

where

$$A_k(z) = A_{kd}\,\mathrm{e}^{\mathrm{i}h_{pk}(z-d_{k-1})} + A_{ku}\,\mathrm{e}^{-\mathrm{i}h_{pk}(z-d_k)}, \quad \widetilde{A}_k(z) = A_{kd}\,\mathrm{e}^{\mathrm{i}h_{pk}(z-d_{k-1})} - A_{ku}\,\mathrm{e}^{-\mathrm{i}h_{pk}(z-d_k)},$$

$$B_k(z) = B_{kd}\,\mathrm{e}^{\mathrm{i}h_{sk}(z-d_{k-1})} + B_{ku}\,\mathrm{e}^{-\mathrm{i}h_{sk}(z-d_k)}, \quad \widetilde{B}_k(z) = B_{kd}\,\mathrm{e}^{\mathrm{i}h_{sk}(z-d_{k-1})} - B_{ku}\,\mathrm{e}^{-\mathrm{i}h_{sk}(z-d_k)},$$

$$C_k(z) = C_{kd}\,\mathrm{e}^{\mathrm{i}h_{sk}(z-d_{k-1})} - C_{ku}\,\mathrm{e}^{-\mathrm{i}h_{sk}(z-d_k)}, \quad \widetilde{C}_k(z) = C_{kd}\,\mathrm{e}^{\mathrm{i}h_{sk}(z-d_{k-1})} + C_{ku}\,\mathrm{e}^{-\mathrm{i}h_{sk}(z-d_k)}.$$

Taking an inverse Fourier transform of the boundary condition (6), three more equations are obtained

$$\mu_1(-2qh_{p1}\widetilde{A}_1(0) - ph_{s1}\widetilde{B}_1(0) + \mathrm{i}q(k_{s1}^2 - 2h_{s1}^2)\widetilde{C}_1(0)) = \sum_{m=0}^{\infty}\hat{\sigma}_{xz\,m}(0)f_m(p), \tag{40}$$

$$\mu_1(-2ph_{p1}\widetilde{A}_1(0) + qh_{s1}\widetilde{B}_1(0) + \mathrm{i}p(k_{s1}^2 - 2h_{s1}^2)\widetilde{C}_1(0)) = \sum_{m=0}^{\infty}\hat{\sigma}_{yz\,m}(0)g_m(p), \tag{41}$$

$$\mu_1((k_{s1}^2 - 2h_{s1}^2)A_1(0) + 2\mathrm{i}h_{s1}(p^2+q^2)C_1(0)) = \sum_{m=0}^{\infty}\hat{\sigma}_{zz\,m}(0)f_m(p). \tag{42}$$

f_m and g_m are defined as

$$f_m(p) = \int_{-a}^{a}\cos p_m y\,\mathrm{e}^{-\mathrm{i}py}\,\mathrm{d}y = \frac{2(-1)^m p\sin(ap)}{p^2 - p_m^2}, \tag{43}$$

$$g_m(p) = \int_{-a}^{a}\sin p_m y\,\mathrm{e}^{-\mathrm{i}py}\,\mathrm{d}y = -\frac{2\mathrm{i}(-1)^m p_m\sin(ap)}{p^2 - p_m^2}. \tag{44}$$

There are two possible methods that can be adopted to express the unknowns in the ground in terms of the constants in the embankment, one of which is the so-called Thomson–Haskell approach or transfer matrix technique [15]. The idea is to obtain a linear relation between the unknowns by recursive elimination, starting from the bottom layer. However, with increasing

frequency the calculations will eventually suffer from precision problems and the algorithm becomes unstable [15]. Instead, to obtain a stable solution algorithm, the global matrix approach used by e.g. Lih and Mal [15] is adopted. The idea is to obtain the unknowns in the ground expressed in the constants in the embankment simultaneously for each p using Eqs. (34)–(42). In this way all the unknowns A_{jd}, A_{ju}, B_{jd}, B_{ju}, C_{jd} and C_{ju} that depend on the continuous Fourier variable p can be expressed in D_{nm} and E_{nm} (which do not depend on p).

Employing an inverse Fourier series with respect to y over the width of the embankment ($-a<y<a$) of the boundary condition (5) together with similar inverse Fourier series of the boundary conditions on top of embankment (9)–(11) the remaining unknowns D_{nm} and E_{nm} are solved. Due to orthogonality there is one equation for each m, denoted with m'. Eqs. (5) result in

$$\frac{1}{2\pi}\int_{-\infty}^{\infty}(\mathrm{i}qA_1(0)+\mathrm{i}pB_1(0)-qh_{s1}C_1(0))f_{m'}(p)\,\mathrm{d}p=\frac{2a}{\varepsilon_{m'}}\hat{u}_{m'}(0),\quad m'=0,1,\ldots, \tag{45}$$

$$\frac{1}{2\pi}\int_{-\infty}^{\infty}(\mathrm{i}pA_1(0)-\mathrm{i}qB_1(0)-ph_{s1}C_1(0))g_{m'}(p)\,\mathrm{d}p=-a\hat{v}_{m'}(0),\quad m'=1,2,\ldots, \tag{46}$$

$$\frac{1}{2\pi}\int_{-\infty}^{\infty}(\mathrm{i}h_{p1}\widetilde{A}_1(0)+(q^2+p^2)\widetilde{C}_1(0))f_{m'}(p)\,\mathrm{d}p=\frac{2a}{\varepsilon_{m'}}\,\hat{w}_{m'}(0),\quad m'=0,1,\ldots. \tag{47}$$

$\varepsilon_{m'}$ is the Neumann factor where $\varepsilon_0=1$ and $\varepsilon_{m'}=2$ for $m'\geqslant 1$. The similar inverse Fourier series are applied on the boundary conditions (9)–(11) resulting in

$$\hat{\sigma}_{zz\,m'}(-d)\,\frac{2a}{\varepsilon_{m'}}=\sum_{m=0}^{\infty}(K_{zb}\Gamma_{m,m'}+K_{zs}\Delta_{m,m'})\hat{w}_m(-d)-\frac{\hat{F}}{c}\,\Gamma_{0,m'},\quad m'=0,1,\ldots, \tag{48}$$

$$\hat{\sigma}_{yz\,m'}(-d)a=\sum_{m=1}^{\infty}K_{yb}\hat{v}_m(-d)\Omega_{m,m'},\quad m'=1,2,\ldots, \tag{49}$$

$$\hat{\sigma}_{xz\,m'}(-d)\,\frac{2a}{\varepsilon_{m'}}=\sum_{m=0}^{\infty}K_{xb}\hat{u}_m(-d)\Gamma_{m,m'},\quad m'=0,1,\ldots, \tag{50}$$

where

$$K_{zb}=-\frac{A_b\rho_b}{c}\,\omega^2+\frac{E_bI_{yb}}{c}\,q^4,\quad K_{zs}=-J_1\omega^2+J_2q^4+J_3q^2p_m^2+J_4p_m^4, \tag{51}$$

$$K_{yb}=-\frac{A_b\rho_b}{c}\,\omega^2+\frac{E_bI_{zb}}{c}\,q^4, \tag{52}$$

$$K_{xb}=-\frac{A_b\rho_b}{c}\omega^2+\frac{E_bA_b}{c}q^2. \tag{53}$$

$\Gamma_{m,m'}$, $\Omega_{m,m'}$ and $\Delta_{m,m'}$ are determined analytically for each combination of m and m':

$$\Gamma_{m,m'}=\int_{-b_R-c/2}^{-b_R+c/2}\cos p_m y\,\cos p_{m'}y\,\mathrm{d}y+\int_{b_R-c/2}^{b_R+c/2}\cos p_m y\cos p_{m'}y\,\mathrm{d}y, \tag{54}$$

$$\Omega_{m,m'} = \int_{-b_R-c/2}^{-b_R+c/2} \sin p_m y \, \sin p_{m'} y \, \mathrm{d}y + \int_{b_R-c/2}^{b_R+c/2} \sin p_m y \sin p_{m'} y \, \mathrm{d}y, \tag{55}$$

$$\Delta_{m,m'} = \int_{-b_S}^{b_S} \cos p_m y \, \cos p_{m'} y \, \mathrm{d}y. \tag{56}$$

Finally the Fourier transformed force in Eq. (40) is

$$\hat{F} = F_0 \int_{-\infty}^{\infty} \int_{-\infty}^{\infty} \delta\left(x - \int_0^t V(s)\,\mathrm{d}s\right) \mathrm{e}^{\mathrm{i}(\omega t - qx)} \,\mathrm{d}x \,\mathrm{d}t. \tag{57}$$

The integration of the velocity within the Dirac delta function is needed if the train accelerates. However, if the train travels with constant speed, V_0 the expression is simplified:

$$\hat{F} = F_0 \int_{-\infty}^{\infty} \int_{-\infty}^{\infty} \delta(x - V_0 t)\, \mathrm{e}^{\mathrm{i}(\omega t - qx)} \,\mathrm{d}x \,\mathrm{d}t = F_0 \, \frac{2\pi}{|V_0|} \, \delta\left(\frac{\omega}{V_0} - q\right). \tag{58}$$

This enables very fast computations, since the inverse Fourier transform with respect to q becomes trivial, i.e. $q = \omega/V_0$ (typically around 1 min for an $200 \times 200\,\mathrm{m}^2$ domain with a frequency content of $0 < f < 3$ Hz).

4. The embankment boundary conditions

To investigate how much the constraints on the sides of embankment (7) affect the displacement fields, a 2D finite element model in plain strain is used and the results are compared to the model with natural boundary condition and to an embankment with sloping sides (to simulate a more natural geometry). The symmetric geometry of the problem is used to reduce the computational time. The computational domain of the model is shown to the left in Fig. 2. The materials in the embankment and in the ground represents the materials that are used in the final model in the embankment and in the surface layer, see further in the next section. The ground is clamped at its outer surface. In this way it is efficient to make a frequency response analysis, using a stationary harmonic loading. Thus a harmonic force with the amplitude $F_0 = 50$ kN and the excitation frequency ω varied between 1 and 40 Hz is applied at the position where the rails are placed, see Fig. 2. Since the solution procedure requires steady-state conditions, enough damping has to be adopted to avoid responses from waves that are reflected by the clamped boundary. A good approximation of the half-infinite domain is obtained if the wave amplitude is less than 90% of the excitation amplitude close to the clamped boundary. Rayleigh damping is used, which models the damping with coefficients proportional to the mass and stiffness matrices $C = \alpha_{dM} M + \beta_{dK} K$. The coefficients are obtained using the constant critical damping $\xi = 0.1$ at the frequencies 1 and 10 Hz from

$$\xi_i = \frac{1}{2}\left(\frac{\alpha_{dM}}{\omega_i} + \beta_{dK}\omega_i\right). \tag{59}$$

This gives $\alpha_{dM} = 1.1424$ and $\beta_{dK} = 0.0029$.

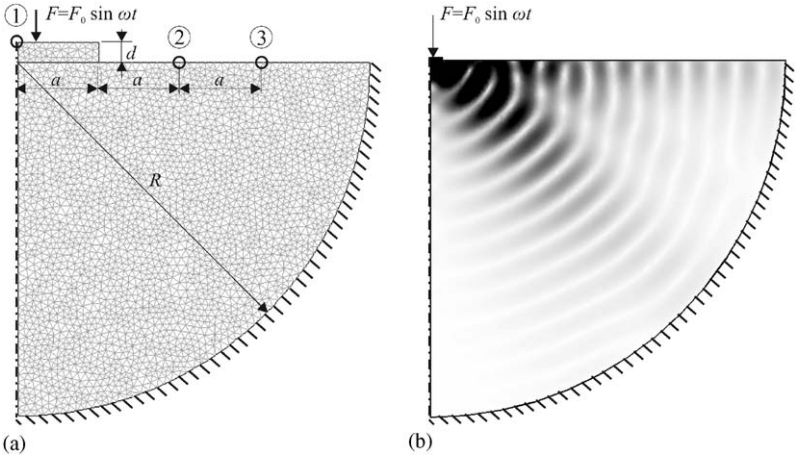

Fig. 2. (a) The principles of a 2D FE-model to simulate the frequency response due to harmonic loading with frequency ω; (b) an example of the total amplitude for the excitation frequency 5 Hz. The wavelength in the ground is 17.4 m resulting in the radius $R = 121.8$ m.

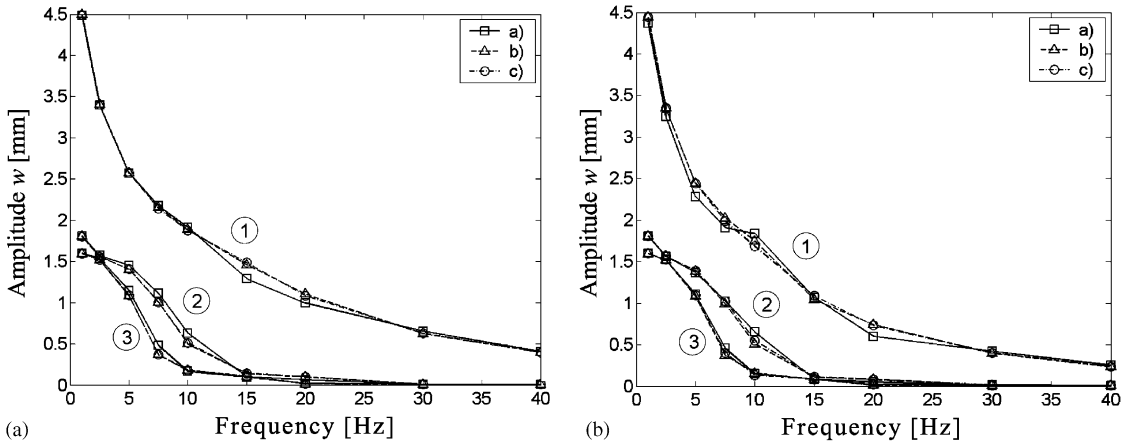

Fig. 3. The resulting vertical amplitudes at the positions 1, 2 and 3 shown in Fig. 2. The results are given for the three models of the embankment in Fig. 4(a)–(c). The height of the embankment is (a) $d = 0.5$ m and (b) $d = 1.0$ m.

The frequency response analysis is made at discrete frequencies between 1 and 40 Hz. The higher the frequency, the faster the waves are damped, so it is unnecessary to use the same domain for all frequencies. Hence the radius of the ground domain is chosen to be $R = 8\lambda$ for low frequencies (less than 5 Hz) and $R = 7\lambda$ for higher frequencies, where λ is the wavelength of the shear wave in the ground for the investigated frequency. To obtain accurate results the maximum edge size of the used triangular elements is chosen in a way so that there are at least six elements per wavelength. The elements are Lagrange–Quadratic elements which give good accuracy.

The vertical displacement amplitudes at the positions 1–3 (see Fig. 2) are gathered for discrete frequencies in Fig. 3 for embankments with $d/2a = \frac{0.5}{8}$ to the left and $d/2a = \frac{1}{8}$ to the right. The

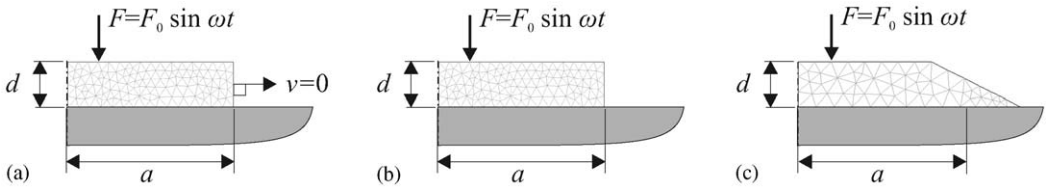

Fig. 4. The three embankments used in the validation of the boundary conditions (7): (a) the embankment used in the presented model; (b) the same rectangular region, but with natural boundary conditions at the sides; (c) an embankment with sloping sides to represent a more common geometry of existing embankments.

solid lines with square markers represent the embankment with unnatural boundary conditions, Fig. 4a, the dashed lines with triangular markers the rectangular embankment with natural boundary conditions, Fig. 4b, and the dash–dotted lines with circular markers the embankment with sloping sides, Fig. 4c. In general it is seen that the approximation with the model (a) gives very good agreement to both model (b) and model (c). There are no significant differences between the three models if the height of the embankment is changed from 0.5 to 1.0 m. At 40 Hz the model (a) disagree at most with 20% with the model (b), which occurs at position 2. To conclude, the constraints on the sides of the embankment give very good approximations of the displacements due to the vertical loading compared to the results obtained with the natural boundary conditions, i.e. with $\sigma_{yy\,e} = 0$ instead of $v_e = 0$. However, if the load was applied transversally, the results would disagree much more.

5. Numerical examples

Madshus and Kaynia [3] use the program "VibTrain" described in Kaynia et al. [2] to predict the ground vibrations observed at the site Ledsgard. They represent the track by a beam with finite elements resting on a layered ground. A similar approach is taken by Takemiya [4], where the track is represented with an Euler–Bernoulli beam. Due to nonlinearities in the soils, the material parameters are highly dependent on the velocity, mainly why two train speeds have been investigated: 70 and 200 km/h. The ground is modelled with five layers ($n = 5$) and the soil parameters adopted for the present model are tabulated in Table 2, based on the comprehensive measurements performed by the Swedish National Rail Administration BANVERKET and used by Kaynia et al. [2], Madshus and Kaynia [3] and Takemiya [4].

Both the geometrical and material properties for the embankment are somewhat uncertain. For the beam used in "VibTrain" Kaynia et al. [2] use the bending stiffness $EI = 200\,\mathrm{MNm}^2$ at low train speeds and $EI = 80\,\mathrm{MNm}^2$ at high speeds, and the mass density is taken as 10 800 kg/m. The geometries for the track in question are vaguely described. However, in the paper presented by Madshus and Kaynia [3], a cross section of a part of the track structure at Ledsgard (consisting of three tracks) is outlined. Assuming that Madshus and Kaynia [3] use a symmetric embankment with the dimensions $1.4 \times 8.0\,\mathrm{m}^2$ to obtain the bending stiffness for their beams, the modulus of elasticity for the embankment is obtained from the given bending stiffness at low and high train speeds (excluding the bending stiffness for the rails).

Table 2
Soil parameters from the test site Ledsgard [3,4], used in the simulations for low train speeds ($V_0 = 70$ km/h) and high train speeds ($V_0 = 200$ km/h)

Soil layer	Thickness (m)	Mass density ρ_j (kg/m^3)	c_s (m/s)		c_p (m/s)		Damping ratio δ_j	
			$V_0 = 70$	$V_0 = 200$	$V_0 = 70$	$V_0 = 200$	$V_0 = 70$	$V_0 = 200$
Surface crust ($j = 1$)	1.1	1500	72	65	500	340	0.04	0.063
Organic clay ($j = 2$)	3.0	1260	41	33	500	360	0.02	0.058
Marine clay ($j = 3$)	4.5	1475	65	60	1500	1500	0.05	0.098
Marine clay ($j = 4$)	6.0	1475	87	85	1500	1500	0.05	0.064
Marine clay ($j = 5$)	∞	1475	100	100	1500	1500	0.05	0.060

Using the material parameters shown in Table 2, the amplitudes become too small at low train speeds when the 1.4 m thick embankment is used, no matter the width of the embankment. Both the average material parameters for the 1.4 m thick embankment consisting of crushed rock, gravel and sand given by Madshus and Kaynia [3] and the bending stiffness used by Kaynia et al. [2] and by Takemiya [4] was used. When the track was replaced by the Euler–Bernoulli beam with the width 3.0 m as Takemiya [4] proposes, the amplitudes agree well at the train speed 70 km/h but disagree much at 200 km/h.

To obtain more realistic results the somewhat arbitrary cross section $0.5 \times 8.0\,\mathrm{m}^2$ for the embankment together with the mass density $\rho_e = 1800\,\mathrm{kg/m}^3$ [3] and the Poisson ratio $v_e = 0.3$ is chosen. It is seen in the next section that with this choice the results agree very well with measurements.

On top of the embankment the rails are placed. They are standard UIC60 rails with cross-sectional area $A_b = 76.87\,\mathrm{cm}^2$, modulus of elasticity $E_b = 210\,\mathrm{GPa}$, density $\rho_b = 7850\,\mathrm{kg/m}^3$ and moment of inertia about the y- and z-axis $I_{yb} = 3055\,\mathrm{cm}^4$ and $I_{zb} = 516.4\,\mathrm{cm}^4$ [16]. The base that is in contact with the embankment is $c = 15\,\mathrm{cm}$ and the span of the rails is $2b_R = 1.5\,\mathrm{m}$, see Fig. 1.

A standard mono-block sleeper coded NS 90 [16] has the outer dimensions $2520 \times 300 \times 233\,\mathrm{mm}^3$ (length × width × height) and are distributed with the regular intervals 0.67 m [3]. In this model the distributed mono-block sleepers are modelled with the transversely isotropic (in the y–z plane) Kirchhoff plate, which has a width of 2520 mm, height of 233 mm and an infinite distribution along the track. The weight of one sleeper is within 200–300 kg, and the average of 250 kg gives the mass density of the plate $\rho_s = 635\,\mathrm{kg/m}^3$. With the modulus of elasticity $E_s = 38\,450\,\mathrm{MPa}$ for one sleeper [17] the stiffness in the y–z plane becomes $E_{sk} = 38\,450\,\mathrm{MPa}$. As the sleepers are supported directly on the gravel on the embankment, the stiffness in the x direction is chosen to be zero, $E_{sx} = 0\,\mathrm{MPa}$, as well as the shear modulus, $G_{sx} = 0\,\mathrm{MPa}$. The Poisson's ratio is assumed to be $v_{syz} = v_{sxk} = 0.2$ with some uncertainty, but experience shows that this does not affect the results (k is any direction perpendicular to the x direction).

The axle-load is introduced via Eqs. (9) and (57)–(58) and in the model it is superimposed to yield an X2 train with five cars, one of which is the engine, see Fig. 5. It has the same configuration as the train that operated along the west coast line during the measurements at Ledsgard [1–4].

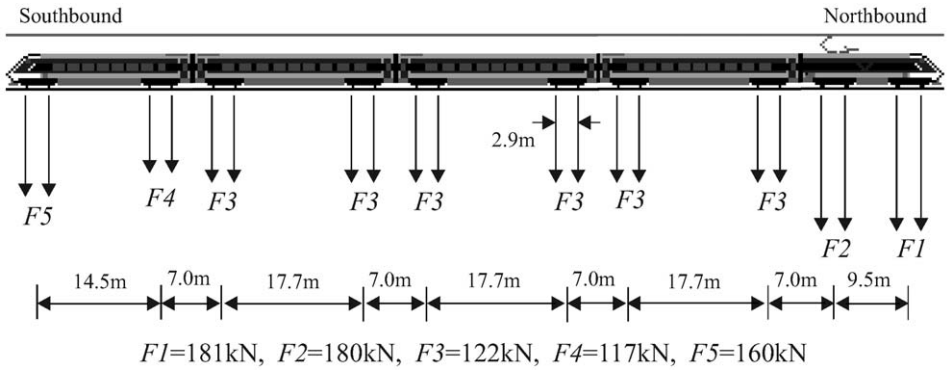

Fig. 5. The X2 train configuration that is used in the model, showing the geometrical properties and the axle-loads $F1$–$F5$.

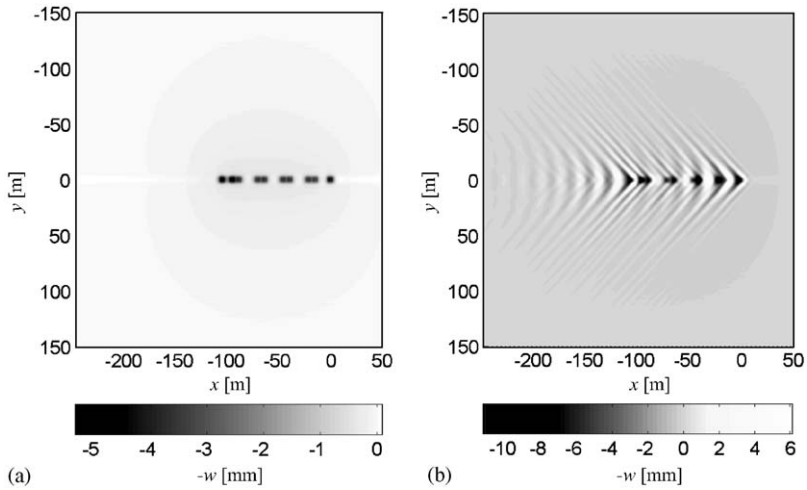

Fig. 6. Simulated vertical ground motion at $z = 0$ for an X2 train in southbound configuration travelling from left to right at the site Ledsgard. The train speeds are: (a) 70 km/h and (b) 200 km/h.

5.1. Simulations at 70 and 200 km/h

Fig. 6 shows the vertical motion of the ground at $z = 0$ when the front of the train passes the origin. The train travels from left to right with 70 km/h (left figure) and 200 km/h (right figure) and the vertical displacement w is displayed in a gray scale. When the train travels with 70 km/h the field is quasi-static, but as the train passes the shear wave velocity for the softest clay ($c_{s2} \approx 148$ km/h), the characteristic mach-cone is formed behind the train.

The same solutions are seen in Fig. 7, but at $y = 0$ and $z = -d$ (the solid lines). In addition the measured displacement is seen as the dashed line. In the left figure the train travels with 70 km/h and the result agrees very well with corresponding measured displacement. However, at the front

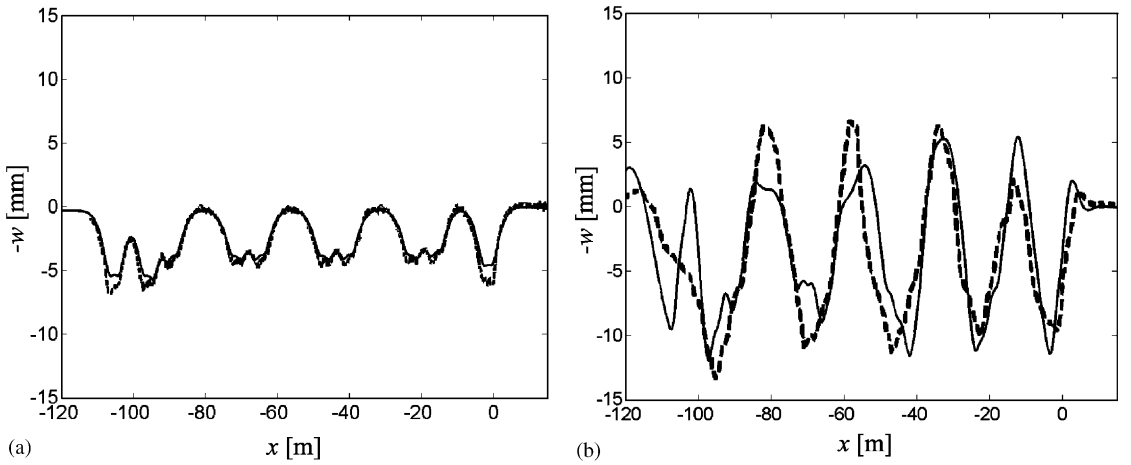

Fig. 7. Simulated (solid curve) and measured (dashed curve) vertical displacement at $y = 0$ and $z = -d$. The train speeds are: (a) 70 km/h and (b) 200 km/h, in southbound direction (travelling from left to right in the figures).

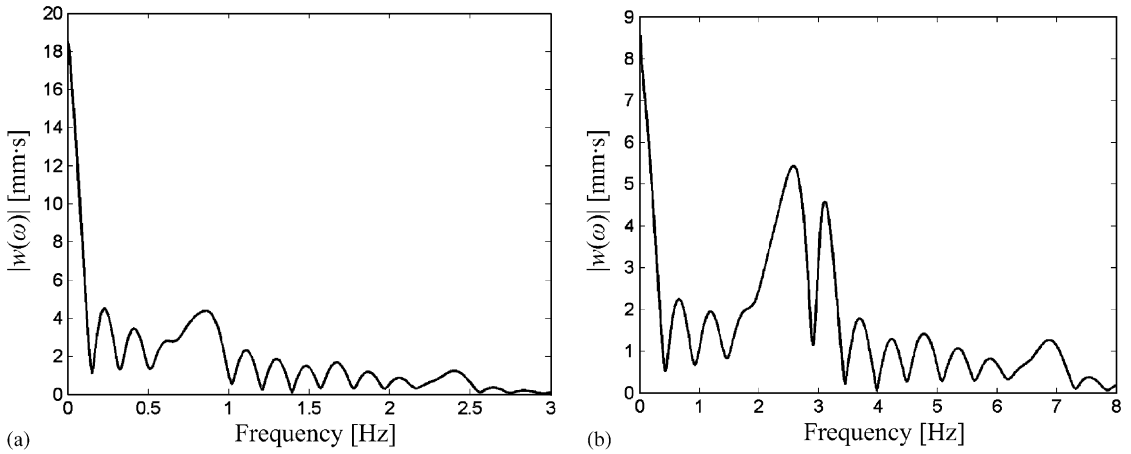

Fig. 8. Frequency spectra for the simulated displacements in Fig. 7. The speeds are: (a) 70 km/h and (b) 200 km/h.

and back wheel pair the levels disagree with more than 1 mm. It should be remarked that it is more or less just the static displacement that follows the train at this velocity and that low frequencies below 3 Hz completely dominate, see Fig. 8. The simulation is made for frequencies up to 10 Hz.

To the right the speed is 200 km/h and also here the simulation is made up to 10 Hz. The simulated displacements differ a bit from the measured results, but still the overall levels agree well. It should be remarked that also Takemiya [4] and Kaynia et al. [2] obtain similar disagreements at 200 km/h. The amplitudes become very large, which emphasize the importance of designing railway lines on grounds with higher shear wave velocities than the operating train

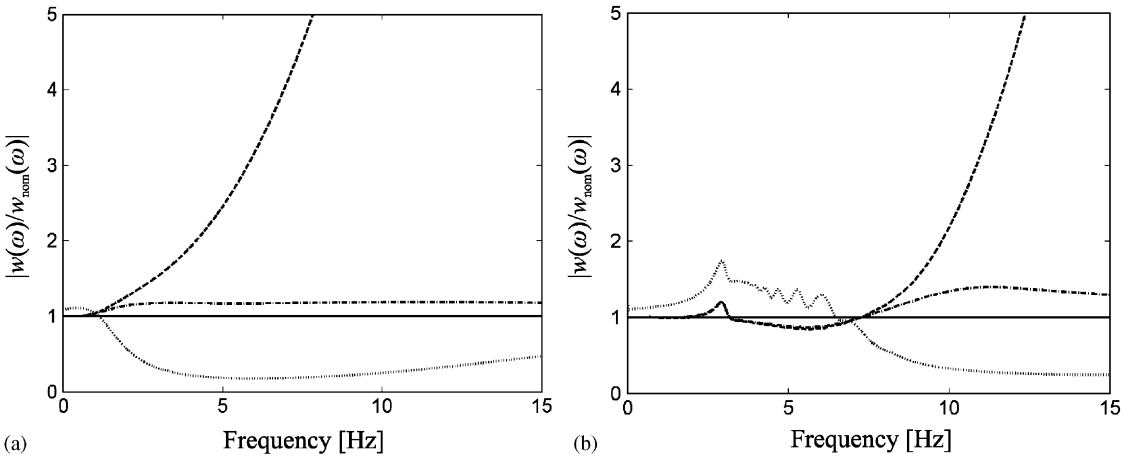

Fig. 9. The quotient between the frequency response for some variations in the track model and the present track model at $y = 0$ and $z = -d$. The solid curve (—) represents the present model, the dashed curve (−−) an embankment without rails and sleepers, the dash–dotted curve (−·) the present model but without the coupling to the rod equation in the longitudinal direction in Eq. (11), i.e. $\sigma_{xz} = 0$ at the interface between the rails and the embankment, and the dotted curve (···) that the track is replaced with an equivalent Euler–Bernoulli beam. The train speeds are: (a) 70 km/h and (b) 200 km/h in southbound direction.

speeds. Countermeasures such as the dry deep mixing method (dry DMM) has been used by BANVERKET at the site Ledsgard with good results.

Fig. 8 shows the corresponding frequency spectra for the displacements at a fixed point on the x axis. They reveal a wave-like pattern with sharp valleys that is due to interference between all the wheel loads [4]. At the speed 70 km/h (the left figure) the static value at 0 Hz is 18.3 mm s and already at 1 Hz the value is less than 12% of this and at 3 Hz less than 3%. When the train speed is increased to 200 km/h (the right figure) the shape of the frequency response is somewhat distorted. The levels for low frequencies are decreased but at higher frequencies they are increased. The interference pattern is stretched out in proportion to the increased speed, which is clearly seen for the sharp valley at 1 Hz at the speed 70 km/h, which is moved to 3 Hz for the speed 200 km/h with a factor of $\frac{200}{70}$. The static value at 0 Hz is here 8.5 mm s and it is not reduced to less than 20% until 3.5 Hz and less than 5% at 7.5 Hz.

In Fig. 9, four curves (at each speed) of the quotient between the frequency response for some variations of the track model and the present track model on top of the embankment at $y = 0$ m are shown. The solid curve is for the present model. The dashed curve shows the response for a track model without rails and sleepers. It is seen already at as low frequencies as 1 Hz for the train speed 70 km/h and 7 Hz for 200 km/h that the higher the frequency is, the more the simplified model overestimates the results compared to the present model. A similar track model as that proposed, but without the coupling in the longitudinal direction between the rails and the embankment in Eq. (11) is represented with the dash–dotted curve. It overestimates the results above 1 and 7 Hz at the speeds 70 and 200 km/h, but the results differ with at most 30% at 70 km/h and 60% at 200 km/h. In comparison to the response from the model with the track replaced with an Euler–Bernoulli beam (dotted curve), the differences are small. The same

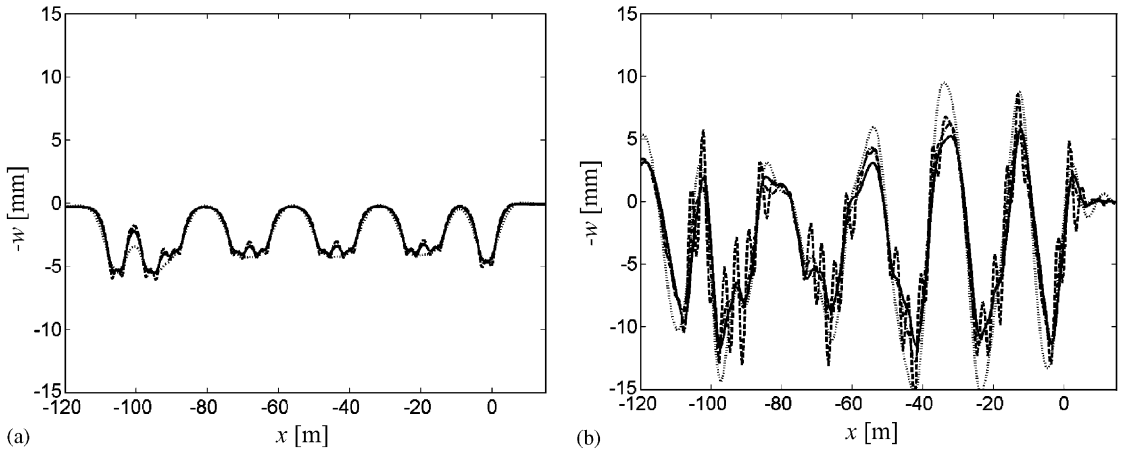

Fig. 10. The time domain displacements for the results in Fig. 9. The solid curve (—) represents the present model, the dashed curve (−−) an embankment without rails and sleepers, the dash–dotted curve (−·) the present model but without the coupling to the rod equation in the longitudinal direction in Eq. (11), i.e. $\sigma_{xz} = 0$ at the interface between the rails and the embankment, and the dotted curve (···) that the track is replaced with an equivalent Euler–Bernoulli beam. The train speeds are: (a) 70 km/h and (b) 200 km/h in southbound direction.

parameters as Takemiya [4] use for the equivalent Euler–Bernoulli beam are adopted here and are represented by the bending stiffness $EI = 200\,\mathrm{MNm}^2$ at 70 km/h and $EI = 80\,\mathrm{MNm}^2$ at 200 km/h, the mass density 10 800 kg/m and the cross-sectional area $1.4 \times 3.0\,\mathrm{m}^2$. Moreover, it is assumed that there is no interaction in the longitudinal direction when the Euler–Bernoulli beam is used. At most the model with the Euler–Bernoulli beam deviates with a factor 9 at 70 km/h and a factor 4 at 200 km/h. For low frequencies, the displacement levels are remarkably higher than the present model. At 70 km/h the differences are almost 10% in the frequency range 0–1 Hz, whereas at 200 km/h the differences are between 10% and 80% higher in the range 0–7 Hz. Mainly at 200 km/h, this appears as higher time domain amplitudes compared to the present model. In Fig. 10 the results from Fig. 9 are shown in the time domain. At 70 km/h, the results are similar for all four models. However, if the train propagates at 200 km/h, the amplitudes differ much more. The solid curve is for the present model, the dashed for the model without rails and sleepers, the dash–dotted for the model without longitudinal coupling to the rails and the dotted for the equivalent Euler–Bernoulli beam. It is clear that the model without rails and sleepers provide a response with a high frequency content, which was seen in Fig. 9 in the comparison to the present model. Also the high displacement levels in the frequency range 0–7 Hz for the Euler–Bernoulli beam is confirmed. However, the response for the model without the longitudinal coupling to the rails is not so clear. Knowing from Fig. 9 that it agrees with the dashed curve up to 7 Hz, one can distinguish that the dash–dotted curve constitutes the mean of the oscillating dashed curve.

It should also be mentioned that the coupling between the embankment and the rails in the transverse direction has been investigated by replacing the boundary condition (10) by $\sigma_{yze} = 0$ and almost no deviation between that model and the present model could be observed.

Finally, to give an example of the importance of the modelling of the ground structure, the thickness of layer 2, i.e. the organic clay layer, was changed from 3.0 to 3.5 m. The results of

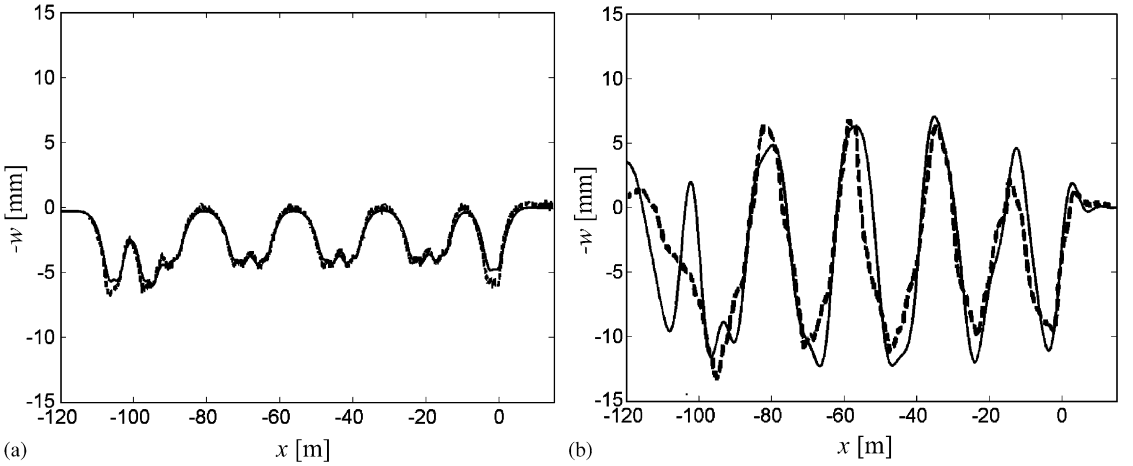

Fig. 11. Simulated (solid curve) and measured (dashed curve) vertical displacement at $y = 0$ and $z = -d$. The train speeds are: (a) 70 km/h and (b) 200 km/h, in southbound direction (travelling from left to right in the figures). On the contrary to Fig. 7 the layer 2 that consist of organic clay is made thicker from 3.0 to 3.5 m.

the track displacements are seen in Fig. 11. The displacements at 70 km/h is slightly better with the modified ground model, but as the speed is changed to 200 km/h the result becomes much more accurate than in Fig. 7. The results are very sensitive to the thickness of at least the layer with the soft organic clay at higher train speeds, which shows the difficulties in eliminating sources of errors in geometrical parameters for the ground. Also the material parameters contribute to uncertainties in the results.

6. Concluding remarks

The somewhat unnatural boundary conditions at the sides of the embankment has been investigated using finite element models and comparing the displacement amplitudes given by those conditions and the natural ones. It is seen that the constraints on the sides give very good approximations of the displacements at least up to 40 Hz when the loads are applied vertically.

The present track-ground model gives very good results at both 70 and 200 km/h. The displacements are compared to measurements performed by the Swedish National Rail Administration, BANVERKET, and at 70 km/h the displacements on top of the track agree almost exactly. But as the train speed is increased to 200 km/h, the simulated track displacements disagree a little. However, if the thickness of the organic clay layer is increased from 3.0 to 3.5 m, the results become very good.

The present track model has also been compared to those with more simplified track models. Since the displacements are dominated by low frequencies (up to 3 Hz) at the speed 70 km/h, the track without rails and sleepers, the track without longitudinal coupling to the rails and the track replaced by an equivalent Euler–Bernoulli beam, all give similar time domain results as the present track model. Yet at higher frequencies than 1 Hz, the simulations made with the track

without rails and sleepers and the equivalent Euler–Bernoulli beam disagree much compared to the present model. At the train speed 200 km/h the track represented by the Euler–Bernoulli beam gives results that disagree much. Because of amplified displacement levels in the frequency range 0–7 Hz, the time domain amplitudes become large. The other track models give reasonably good displacement levels up to about 7.5 Hz.

Due to simplifications such as no dynamics in the train, no inhomogeneities in the contact between the rails and the wheels and no inhomogeneities in the ground, some important sources that generate ground borne vibrations have not been considered. Therefore, some high frequency mechanisms are disregarded.

Acknowledgements

This work is part of the activities at the Center of Excellence CHARMEC (CHAlmers Railway MEChanics, www.charmec.chalmers.se). We would like to thank Mr. Alexander Smekal at the Swedish National Rail Administration BANVERKET and Dr. Torbjörn Ekevid, who has provided us with measurement data from the site Ledsgard.

References

[1] K. Adolfsson, B. Andréasson, P.R. Bengtsson, P. Zackrisson, High speed train X2000 on soft organic clay—measurements in Sweden, in: Barends, et al. (Eds.), *Proceeding of the 12th European Conference on Soil Mechanics and Geotechnical Engineering*, vol. 3, Balkema, Rotterdam, 1999, pp. 1713–1718.

[2] A.M. Kaynia, C. Madshus, P. Zackrisson, Ground vibration from high-speed trains: prediction and countermeasure, *Journal of Geotechnical and Geoenvironmental Engineering* 126 (6) (2000) 531–537.

[3] C. Madshus, A.M. Kaynia, High-speed railway lines on soft ground: dynamic behaviour at critical train speed, *Journal of Sound and Vibration* 231 (3) (2000) 689–701.

[4] H. Takemiya, Simulation of track-ground vibrations due to a high-speed train: the case of X2000 at Ledsgard, *Journal of Sound and Vibration* 261 (3) (2003) 503–526.

[5] F.C.P. de Barros, J.E. Luco, Response of a layered viscoelastic half-space to a moving point load, *Wave Motion* 19 (2) (1994) 189–210.

[6] M.C.M. Bakker, M.D. Verweij, B.J. Kooij, H.A. Dieterman, The traveling point load revisited, *Wave Motion* 29 (2) (1999) 119–135.

[7] A.T. de Hoop, The moving-load problem in soil dynamics—the vertical displacement approximation, *Wave Motion* 36 (4) (2002) 335–346.

[8] H.A. Dieterman, A. Metrikine, The equivalent stiffness of a half-space interacting with a beam. Critical velocities of a moving load along the beam, *European Journal of Mechanics—A/Solids* 15 (1) (1996) 67–90.

[9] V. Krylov, C. Ferguson, Calculation of low-frequency ground vibrations from railway trains, *Applied Acoustics* 42 (3) (1994) 199–213.

[10] X. Sheng, C.J.C. Jones, M. Petyt, Ground vibration generated by a harmonic load acting on a railway track, *Journal of Sound and Vibration* 225 (1) (1999) 3–28.

[11] T. Ekevid, N.-E. Wiberg, Wave propagation related to high-speed train: a scaled boundary FE-approach for unbounded domains, *Computer Methods in Applied Mechanics and Engineering* 191 (36) (2002) 3947–3964.

[12] J.P. Wolf, C. Song, The scaled boundary finite-element method—a primer: derivations, *Computers & Structures* 78 (1–3) (2000) 191–210.

[13] A.V. Vostroukhov, A.V. Metrikine, Periodically supported beam on a visco-elastic layer as a model for dynamic analysis of a high-speed railway track, *International Journal of Solids and Structures* 40 (21) (2003) 5723–5752.

[14] S.A. Ambartsumyan, *Theory of Anisotropic Plates*, vol. II, Technomic Publication, Stanford, USA, 1970.
[15] S.-S. Lih, A.K. Mal, On the accuracy of approximate plate theories for wave field calculations in composite laminates, *Wave Motion* 21 (1) (1995) 17–34.
[16] C. Esveld, *Modern Railway Track*, MRT-Productions, Duisburg, West Germany, 1989.
[17] G. Kumaran, D. Menon, K.K. Nair, Dynamic studies of railtrack sleepers in a track structure system, *Journal of Sound and Vibration* 268 (3) (2003) 485–501.